

Electric-Field Control of Ferromagnetism in Mn-Doped ZnO Nanowires

Li-Te Chang,[†] Chiu-Yen Wang,^{‡,§,||} Jianshi Tang,^{†,||} Tianxiao Nie,[†] Wanjun Jiang,[†] Chia-Pu Chu,[†] Shamsul Arafin,[†] Liang He,[†] Manekkathodi Afsal,[‡] Lih-Juann Chen,^{*,‡} and Kang L. Wang^{*,†}

[†]Device Research Laboratory, Department of Electrical Engineering, University of California, Los Angeles, California 90095, United States

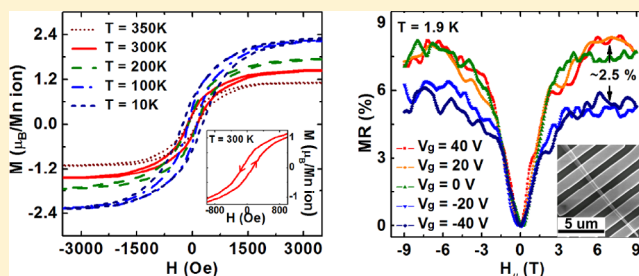
[‡]Department of Materials Science and Engineering, National Tsing Hua University, Hsinchu, Taiwan 30013, Republic of China

[§]Department of Materials Science and Engineering, National Taiwan University of Science and Technology, Taipei, Taiwan 10607, Republic of China

S Supporting Information

ABSTRACT: In this Letter, the electric-field control of ferromagnetism was demonstrated in a back-gated Mn-doped ZnO (Mn-ZnO) nanowire (NW) field-effect transistor (FET). The ZnO NWs were synthesized by a thermal evaporation method, and the Mn doping of 1 atom % was subsequently carried out in a MBE system using a gas-phase surface diffusion process. Detailed structural analysis confirmed the single crystallinity of Mn-ZnO NWs and excluded the presence of any precipitates or secondary phases. For the transistor, the field-effect mobility and n-type carrier concentration were estimated to be $0.65 \text{ cm}^2/\text{V}\cdot\text{s}$ and $6.82 \times 10^{18} \text{ cm}^{-3}$, respectively. The magnetic hysteresis curves measured under different temperatures ($T = 10\text{--}350 \text{ K}$) clearly demonstrate the presence of ferromagnetism above room temperature. It suggests that the effect of quantum confinements in NWs improves T_c , and meanwhile minimizes crystalline defects. The magnetoresistance (MR) of a single Mn-ZnO NW was observed up to 50 K. Most importantly, the gate modulation of the MR ratio was up to 2.5 % at 1.9 K, which implies the electric-field control of ferromagnetism in a single Mn-ZnO NW.

KEYWORDS: Diluted magnetic semiconductor, Mn-doped ZnO, nanowire, carrier-mediated ferromagnetism, quantum confinement



Spintronics, utilizing electron spin as a new degree of freedom for information processing, has emerged as a promising solution for the challenges of continuous scaling of CMOS technology.¹ Spin field-effect-transistor^{2–4} (spin-FET) aims to meet the requirements of novel electronic devices, including ultrahigh density, low power consumption, and nonvolatility. There are spin-FETs to manipulate spin transport by a gate voltage through the Rashba effect² or to modulate spin-polarized carriers by the magnetization configuration (parallel or antiparallel) of half-metallic source and drain.³ Beyond those, the ferromagnetic phase change could also be used as a state variable to minimize the charge current dissipation. One of the approaches is to manipulate the ferromagnetism in a diluted magnetic semiconductor (DMS) channel by a gate voltage, called nonvolatile transpinor device, which controls the communication between the source/drain terminals through the exchange interaction.^{4,5}

Previously, Dietl⁶ applied the Zener model to predict room temperature ferromagnetism (RT-FM) in Mn-doped compound semiconductor, and Mn-ZnO became one of the most promising DMS materials for spintronics for which could function at RT. In 2003, Sharma et al.⁷ first demonstrated the RT-FM in Mn-ZnO thin film, but Kundaliya et al.⁸ argued that

the origin of RT-FM was due to oxygen-vacancy-stabilized phases. To clarify this controversy, in 2005 Coey et al.⁹ proposed a spin-split impurity band model to explain the RT-FM in Mn-ZnO, and many other groups subsequently reported high temperature FM ($T_c > 400 \text{ K}$) in Mn-ZnO thin film^{10–12} and NWs.¹³ They claimed that the high T_c was due to electrons from shallow donor impurities, which form magnetic polaron and a spin-split impurity band.⁹ However, a comprehensive study of the electric-field control of FM has not been reported yet, particularly in the nanoscale material system.

Only recently, Xiu et al.⁴ have used quantum confinement in quantum dots to enhance the exchange interaction between the confined carriers and the Mn dopants, and hence improve T_c in Mn-doped Ge quantum dots; likewise Tang et al.⁵ have demonstrated the spin injection and detection in $\text{Mn}_3\text{Ge}_3/\text{Ge}/\text{Mn}_5\text{Ge}_3$ nanowires transistors. For Mn-ZnO NWs, it have been shown to have better crystallinity by taking advantages of the well-developed synthesis process of ZnO nanostructure¹⁴ as well as the high solubility of 3d metals in ZnO.¹⁵ In this work,

Received: December 3, 2013

Revised: February 11, 2014

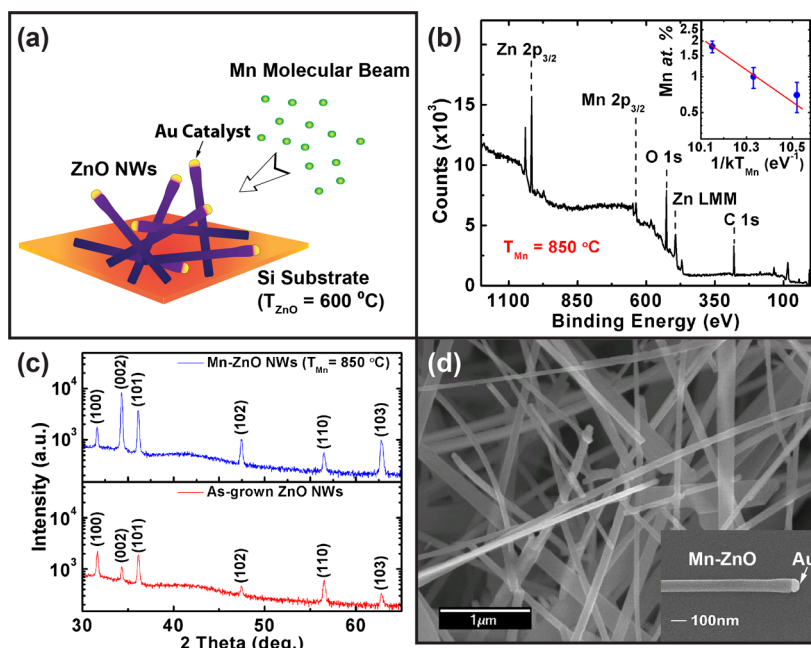


Figure 1. (a) Schematic illustration of doping process utilizing the technique of gas-phase surface diffusion. (b) XPS spectrum of Mn-ZnO NWs. The inset shows the Arrhenius plot of the Mn atomic concentration (x_{Mn}) and T_{Mn} , in which the x_{Mn} is estimated from the high-resolution XPS spectra of Mn 2p_{3/2} and Zn 2p_{3/2} peaks given in Supporting Information Figure S1. (c) XRD data of Mn-ZnO (upper) and as-grown ZnO NWs (lower), respectively. (d) SEM image of an assembly of Mn-ZnO NWs. The inset shows the high-magnification SEM image of a single Mn-ZnO NW, whose diameter is around 70 nm with a gold catalyst on the top.

we report the studies of Mn-ZnO NWs from material characterizations to electrical and magneto-transport measurements. The clear $M-H$ hysteresis loop of an assembly of Mn-ZnO NWs was observed up to 350 K, and meanwhile the magnetoresistance (MR) ratio was measured up to 50 K. More importantly, by using a typical back-gated transistor structure, the effective manipulation of FM of a single Mn-ZnO NW was clearly observed at 1.9 K, which sets the stage for RT spin-FET devices in the future.

Results and Discussion. Zinc oxide nanowires (ZnO NWs) were synthesized on a (100) Si substrate using a traditional thermal evaporation method.¹⁶ The doping process was subsequently carried out in a molecular beam epitaxy (MBE) system. The growth was done at 800°C with a Mn concentration (x_{Mn}) < 2 atom % in order to avoid precipitates, because the thermal equilibrium solubility of Mn in ZnO is predicted up to 25 atom % at 800°C .¹⁵ Under this doping level, the Mn-doped ZnO can be treated as a DMS due to the exchange interaction between magnetic ions. Figure 1(a) is a schematic illustration of the doping process. As-grown ZnO NWs were first rinsed in acetone for 10 min and then loaded into a MBE chamber with a base pressure of 10^{-10} torr. To help Mn diffusion and avoid the secondary phase formation, the Mn deposition lasted for 2 hours. The effusion cell temperature of Mn source was controlled to yield a nominal Mn deposition thickness of 0.7, 1.4, and 2.5 nm, respectively. During the doping process, ZnO NWs were also heated up to 600°C so that the incident Mn atoms could diffuse into ZnO NWs from the surface through gas-phase surface diffusion.^{17,18} After the doping process, the substrate was cooled down to room temperature.

To estimate the Mn concentration, X-ray photoelectron spectroscopy (XPS) was performed on Mn-ZnO NWs with different Mn source temperature (T_{Mn}). Figure 1b shows the

XPS spectrum of Mn-ZnO NWs for $T_{\text{Mn}} = 850^\circ\text{C}$, in which each element peak (Zn, Mn, and O) is clearly observed. The inset shows the Arrhenius plot of the relation between T_{Mn} and x_{Mn} , which is estimated from the high-resolution XPS spectra for Zn 2p_{3/2} and Mn 2p_{3/2} peaks (as shown in Supporting Information Figure S1) from the following equation¹⁹

$$x_{\text{Mn}} = \frac{\frac{I_{\text{Mn } 2p_{3/2}}}{\text{RSF}_{\text{Mn } 2p_{3/2}}}}{\frac{I_{\text{Mn } 2p_{3/2}}}{\text{RSF}_{\text{Mn } 2p_{3/2}}} + \frac{I_{\text{Zn } 2p_{3/2}}}{\text{RSF}_{\text{Zn } 2p_{3/2}}}} \quad (1)$$

where $I_{\text{Mn } 2p_{3/2}}$ and $I_{\text{Zn } 2p_{3/2}}$ are integrated areas under the Mn 2p_{3/2} and Zn 2p_{3/2} peaks in the high-resolution XPS spectra; $\text{RSF}_{\text{Mn } 2p_{3/2}} = 1.77$ and $\text{RSF}_{\text{Zn } 2p_{3/2}} = 3.73$ are the relative sensitivity factors for Mn 2p_{3/2} and Zn 2p_{3/2} peaks,²⁰ respectively. On the other hand, the binding energy of the Mn 2p_{3/2} peak located at 641 eV confirms that the Mn atoms substitute the Zn positions as the Mn²⁺ valence state.²¹ In the following, we will focus on Mn-ZnO NWs with $x_{\text{Mn}} \sim 1$ atom %.

Figure 1c presents the X-ray diffraction (XRD) data for Mn-ZnO (upper) and as-grown ZnO (lower) NWs, respectively. The peak positions from both samples are consistent, which are related to certain crystal planes. No peak from secondary phase formation is observed within the resolution limit of XRD, which indicates the ideal crystalline structure after doping process. Figure 1d is a SEM image of an assembly of Mn-ZnO NWs, and the inset shows a magnified image of a single Mn-ZnO NW with a gold catalyst on the top. These pictures show that the NWs possess a smooth surface with several micrometer lengths and 70 nm diameters.

To further inspect the presence of Mn precipitates if any, as well as the detailed crystal structure in Mn-ZnO NWs,

transmission electron microscopy (TEM) is used. Figure 2a shows the TEM image of a typical Mn-ZnO NWs with [0001]

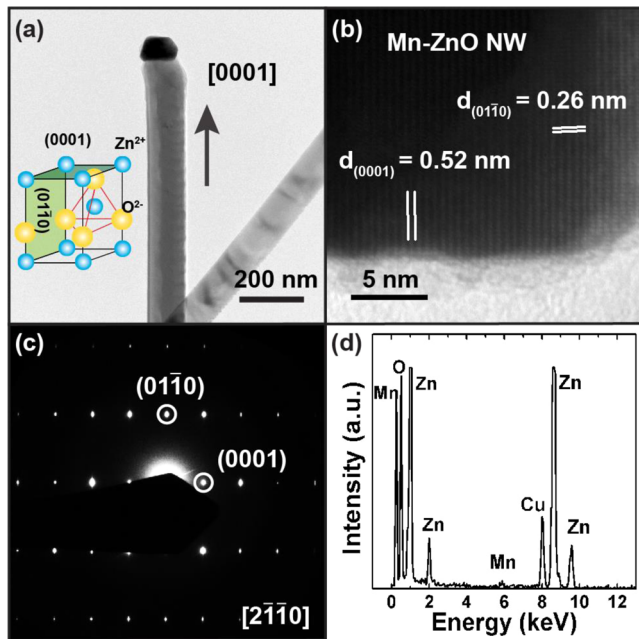


Figure 2. Structural characterization of Mn-ZnO NWs. (a) Low-magnification TEM image of Mn-ZnO NWs growing along [0001] direction. The inset shows the schematic illustration of wurtzite ZnO structure. (b) High-resolution TEM image at Mn-ZnO NW edge confirming its crystalline structure. (c) The corresponding diffraction pattern of Mn-ZnO NWs along the $[2\bar{1}\bar{1}0]$ zone axis. (d) EDS spectrum of the Mn-ZnO NWs. The estimated Mn atomic concentration is 0.5–1.2 atom %.

growth direction. The high-resolution TEM (HR-TEM) image in Figure 2b demonstrates that the Mn-ZnO is single crystalline without the formation of Mn clusters (MnO_x). The lattice spacings are determined to be $d_{(0001)} = 0.52$ nm for (0001) planes and $d_{(01\bar{1}0)} = 0.26$ nm for (01 $\bar{1}0$) planes, respectively. The corresponding lattice parameters could be obtained as $c = d_{(0001)} = 0.52$ nm and $a = d_{(01\bar{1}0)}/\sin 60^\circ = 0.32$ nm in which both parameters are consistent with the typical value of wurtzite zinc oxide^{14,22} ($c = 0.5207$ nm, $a = 0.3296$ nm). Furthermore, the diffraction pattern along the $[2\bar{1}\bar{1}0]$ zone plane in Figure 2c reveals the Mn-ZnO (0001) and (01 $\bar{1}0$) lattice planes as an evidence for the good crystallinity. Then the energy-dispersive spectrum (EDS) in Figure 2d was subsequently taken in situ with TEM, which confirms the x_{Mn} to be 0.5–1.2 atom %. The Cu peak in the EDS spectrum came from the carbon-coated copper grid.

The above XPS and XRD studies were carried out for an assembly of Mn-ZnO NWs, so both spectra provide averaged structural properties of the Mn-ZnO NWs. In order to investigate the transport properties of individual NWs for future device applications, we fabricated back-gated Mn-ZnO NW FET and demonstrated the transistor characteristics at room temperature in Figure 3. To make back-gated Mn-ZnO NW FET, the NWs were first transferred onto a prepatterned $\text{SiO}_2/\text{p}^+\text{-Si}$ substrate, followed by electron beam lithography to pattern multiple electrodes. Before the metal deposition, the sample was dipped in diluted HF ($\text{HF}/\text{H}_2\text{O} = 1:10^6$) for 5 sec to reduce the contact resistance. After electron beam deposition of Ti/Au (10/120 nm) and lift-off process in hot acetone, a

layer of 20 nm Al_2O_3 was subsequently deposited on top using atomic layer deposition (ALD) at 250 °C to passivate the Mn-ZnO NW surface. Previously, it was reported that the surface conductivity of ZnO could dramatically change with different gas adsorption;^{23–25} therefore, the ALD Al_2O_3 step is one of the key steps to make a robust Mn-ZnO NW FET when exposing in ambient. In addition, the low-temperature annealing during ALD process helps to form good ohmic contacts because a heavily doped region ($\text{n}^+\text{-MnZnO}$) is formed next to the Ti/Mn-ZnO interface.^{26–28} As shown in Supporting Information Figure S2a, the source/drain current (I_{ds}) was improved by 3 orders of magnitude after the ALD process (solid circle).

Figure 3a shows the results from both two-probe and four-probe I – V measurements at room temperature in order to exclude the contact resistance. The inset shows a SEM image of a typical Mn-ZnO NW with an effective channel length of 700 nm and a diameter of 70 nm. The resistivity of the Mn-ZnO NW was estimated to be $\rho \sim 1.41 \Omega\cdot\text{cm}$. The inset of Figure 3b is the schematic illustration of a back-gated Mn-ZnO NW FET. Both $I_{\text{ds}}-V_{\text{gs}}$ characteristics in Figure 3b and $I_{\text{ds}}-V_{\text{ds}}$ characteristics at various gate voltages in Figure 3c confirm that majority carriers in Mn-ZnO NWs are n-type. The maximum transconductance ($g_{\text{m}} \equiv dI_{\text{ds}}/dV_{\text{gs}}$) at a source/drain voltage of $V_{\text{ds}} = 20$ mV was extracted to be 7.8×10^{-11} S, which leads to a field-effect electron mobility $\mu = 0.65 \text{ cm}^2/\text{V}\cdot\text{s}$ and electron density $n = 6.82 \times 10^{18} \text{ cm}^{-3}$, respectively. This is calculated by using following equations: $\mu = g_{\text{m}}L^2/V_{\text{ds}}C_{\text{ox}}$ and $n = 1/\rho q\mu$, where $L = 700$ nm is the effective channel length, and the gate capacitance C_{ox} is estimated from the cylinder-on-plate model:²⁶ $C_{\text{ox}} = 2\pi\epsilon_{\text{ox}}\epsilon_0 L/\cosh^{-1}[(r + t_{\text{ox}})/r]$, where $\epsilon_0 = 8.85 \times 10^{-14} \text{ F/cm}$ is the vacuum dielectric constant, $\epsilon_{\text{ox}} = 3.9$ is the relative dielectric constant for SiO_2 , $r = 35$ nm is the radius of the Mn-ZnO NW, and $t_{\text{ox}} = 300$ nm is the thickness of the back-gated dielectric. The calculated gate capacitance would be $C_{\text{ox}} = 2.91 \times 10^{-17} \text{ F}$. It should be pointed out that the cylinder-on-plate model tends to overestimate the gate capacitance; therefore, the value of $\mu = 0.65 \text{ cm}^2/\text{V}\cdot\text{s}$ is the lower limit of the carrier mobility.²⁶ The mobility and carrier concentration measured from 20 devices range from $\mu = 3.55 \text{ cm}^2/\text{V}\cdot\text{s}$, $n = 0.78 \times 10^{18} \text{ cm}^{-3}$ to $\mu = 0.65 \text{ cm}^2/\text{V}\cdot\text{s}$, $n = 6.82 \times 10^{18} \text{ cm}^{-3}$. All devices exhibit n-type behaviors with an overall decrease in mobility but increase in carrier concentration after Mn doping, which is consistent with results from Mn-doped ZnO thin films as reported by Mukherjee et al.¹²

To extract the Schottky barrier height for the Ti contact to Mn-ZnO NWs, temperature-dependent I – V measurements were performed on a Mn-ZnO NW FET in the temperature range of $T = 250$ – 350 K, as shown in Supporting Information Figure S2b. The linear fitting of $\ln(I/T^2)$ versus $1000/T$ in Arrhenius plot at various drain biases in Supporting Information Figure S2c reveals a consistent Schottky barrier height of $q\psi_{\text{SB}} = 30 \pm 2$ meV by assuming that the circuit model of Ti/Mu-ZnO/Ti heterostructure are represented by two back-to-back Schottky diodes, as shown in the inset of Supporting Information Figure S2b. Figure 3d shows the corresponding energy band diagram of a Ti/Mn-ZnO/Ti heterostructure under zero bias, assuming the band structure parameters (such as band gap and electron affinity) of Mn-ZnO are the same as those of nondoped ZnO crystal.²⁹ In the band diagram, Ti forms a very low Schottky barrier ($q\psi_{\text{SB}} = 0.03$ eV) with the Mn-ZnO surface because the work function of Ti ($q\phi_{\text{Ti}} = 4.3$ eV) is closed to the electron affinity of Mn-ZnO

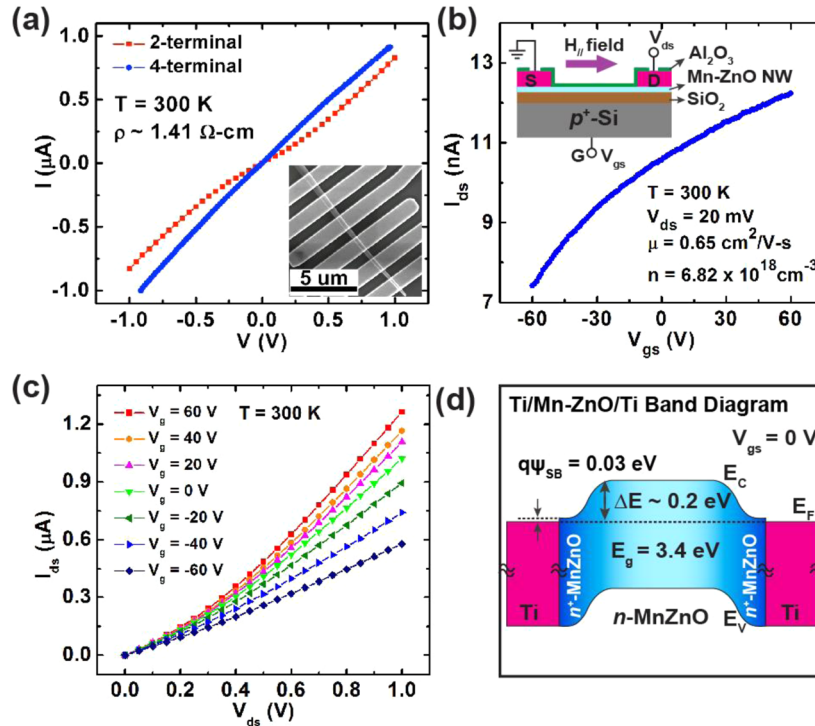


Figure 3. Characterization of a back-gated Mn-ZnO NW FET at room temperature. (a) Two-probe and four-probe I – V measurements of a single Mn-ZnO NW. The inset shows a SEM image of a typical Mn-ZnO NW device with six electrodes. The extracted resistivity is $\rho \sim 1.41 \, \Omega \cdot \text{cm}$. (b) The corresponding I_{ds} – V_{gs} characteristic at $V_{\text{ds}} = 20 \, \text{mV}$. The extracted field-effect mobility is $\mu = 0.65 \, \text{cm}^2/\text{V}\cdot\text{s}$, and the carrier density is $n = 6.82 \times 10^{18} \, \text{cm}^{-3}$. The inset shows the schematic illustration of a back-gated Mn-ZnO NW FET, in which the magnetic field (H_{\parallel}) was applied along the nanowire axial direction. (c) The corresponding I_{ds} – V_{ds} characteristics at various gate voltages. (d) Energy band diagram of a Ti/Mn-ZnO/Ti heterostructure while $V_{\text{gs}} = 0$. ($q\phi_{\text{Ti}} = 4.3 \, \text{eV}$ and $\chi_{\text{MnZnO}} = 4.0 \, \text{eV}$).

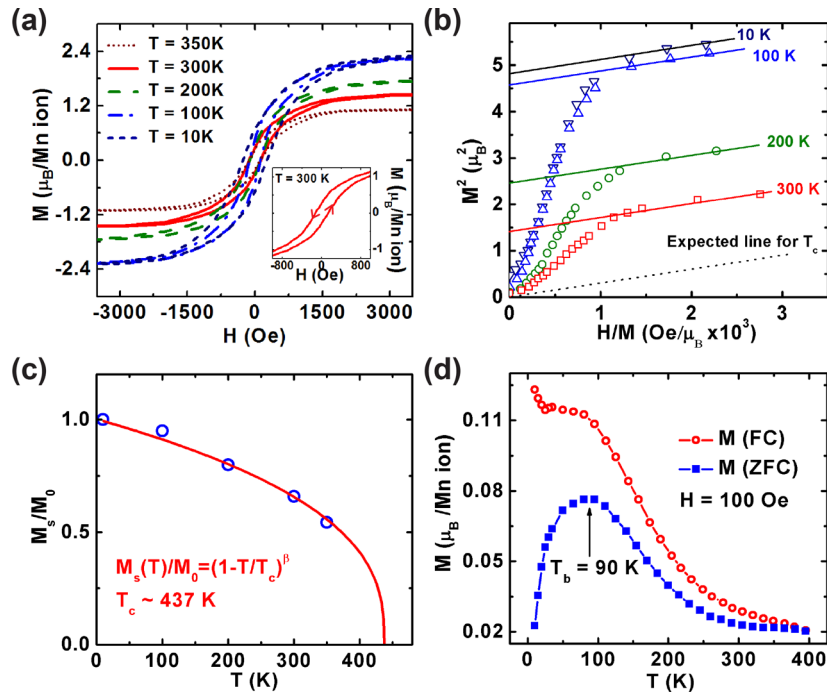


Figure 4. SQUID measurements of an assembly of the Mn-ZnO NWs. (a) Magnetic moment as a function of field for an assembly of Mn-ZnO NWs at $T = 10, 100, 200, 300$, and $350 \, \text{K}$. The inset shows the magnified hysteresis loop near the origin of Mn-ZnO NWs at $300 \, \text{K}$. The red arrows show the sweeping direction of the magnetic field. (b) The Arrott plots of the data in (a). The T_c is projected to be above $300 \, \text{K}$. (c) The normalized saturation magnetization (M_s/M_0) as a function of temperature. The power-law fitting ($\beta = 0.365$) approximately predicts the Curie temperature (T_c) to be $437 \, \text{K}$. (d) Magnetic moment as a function of temperature following FC and ZFC at $H = 100 \, \text{Oe}$, in which the blocking temperature is $T_b = 90 \, \text{K}$.

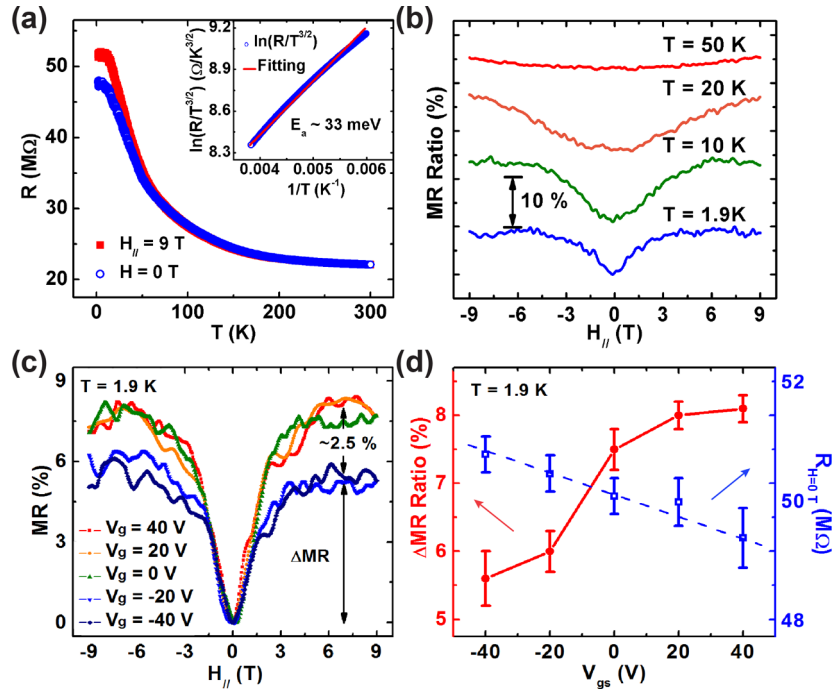


Figure 5. Temperature-dependent magneto-transport measurements on a single Mn-ZnO NW. (a) Temperature-dependent resistance (R – T) measurements on a single Mn-ZnO NW under an axial magnetic fields ($H_{||}$) of 9 T (solid square) and 0 T (open circle). The inset shows the linear fitting for activation energy, $E_a \sim 33$ meV. (b) Magnetoresistance (MR) ratio as a function of $H_{||}$ at different temperature. The MR curves are intentionally shifted for clarity, and the height of the double head arrow represents 10 % of the MR ratio. (c) MR ratio as a function of $H_{||}$ under different gate voltage at 1.9 K, in which ΔMR is defined as the height of the MR curves. (d) The left axis shows the extracted ΔMR (solid circle), and the right axis shows the zero-field resistance (open square) under each gate voltage.

($\chi_{\text{MnZnO}} = 4.0$ eV). Furthermore, since Ti has a higher electron affinity to oxygen, compared with Zn, oxygen atoms tend to diffuse toward the Ti surface and create vacancies, which contribute to additional n -type carriers and result in a heavily doped region (n^+ -MnZnO) next to the Ti/Mn-ZnO interface.²⁸ In addition, the Fermi level is estimated to be 0.2 eV below the conduction band edge using the effective density of states ($N_c = N_v \sim 2 \times 10^{20} \text{ cm}^{-3}$) and carrier concentration ($n = 6.82 \times 10^{18} \text{ cm}^{-3}$) calculated above.

The magnetic properties of the Mn-ZnO NWs were measured by using a Quantum Design superconducting quantum interference device (SQUID). It is noted that samples were carefully handled with nonmagnetic tweezers, capsules, and tapes to avoid contamination. The diamagnetic contribution from the Si substrate has been subtracted and the magnetization is normalized to Bohr magneton per Mn ion ($\mu_B/\text{Mn ion}$) assuming that Mn atoms are homogeneously doped in ZnO NW with a typical wurtzite structure, so the numbers of Mn ions could be estimated from the weight of Mn-ZnO NWs and Mn atomic ratio. Figure 4a shows the M – H hysteresis loops measured at $T = 10, 100, 200, 300$, and 350 K for an assembly of Mn-ZnO NWs. The inset shows the magnified hysteresis loop near the origin at 300 K, in which the magnetic hysteresis, saturation magnetization (M_s) and coercivity field (H_c) are taken as the important features of ferromagnetism. The extracted M_s is $2.2 \mu_B/\text{Mn ion}$ at 10 K, and reduces to $1.4 \mu_B/\text{Mn ion}$ at 300 K. Both values are smaller than the theoretical value of $5 \mu_B/\text{Mn ion}$ of Mn^{2+} state;^{6,7} however, it is consistent with the previous reports of Mn-doped ZnO thin film ($2.2 \mu_B/\text{Mn ion}$ with $n = 3.5 \times 10^{18} \text{ cm}^{-3}$)¹¹ and Mn-doped ZnO NWs ($0.3 - 1.2 \mu_B/\text{Mn ion}$ with $x_{\text{Mn}} = 1 - 4$

atom %)¹³ at 300 K as well as other diluted magnetic semiconductor.⁴

To approximately estimate the Curie temperature (T_c) of the Mn-ZnO NWs, the M – H curves at different temperatures are plotted as M^2 versus H/M , called Arrott plots. By neglecting the high order terms, the relation between H and M could be expressed as^{4,30} $H/M = 1/\chi + \alpha M^2$ where χ is the susceptibility, and α is a materials-dependent constant. When extrapolate each curve to $M^2 = 0$, the T_c is obtained when $1/\chi = 0$. As shown in Figure 4b, the intercept of H/M axis does not vanish ($1/\chi \neq 0$) even at $T = 300$ K, which means that the T_c has not been reached yet.⁴ By using the slope obtained at 300 K, a dash line that passing through origin point could be drawn at the T_c , which is projected to be above 300 K. On the other hand, the temperature dependence of the saturation magnetization is shown in Figure 4c. These data also enable an approximate prediction of the T_c using a power-law equation from the critical behavior model³¹

$$\frac{M_s(T)}{M_0} = \left(1 - \frac{T}{T_c}\right)^\beta \quad (2)$$

where $M_0 \equiv M_s(T = 0) \sim M_s(T = 10 \text{ K})$, and $\beta = 0.365$ is the critical exponent in the 3D Heisenberg model.³² In the figure, the theoretical fitting (solid line) agrees well with the experimental results (empty circles), and shows the $T_c = 437$ K at the intersect of x -axis.

The temperature-dependent magnetization measurement is exhibited in Figure 4d via zero-field cooling (ZFC) and field cooling (FC) at $H = 100$ Oe. The ZFC and FC curves show a typical ferromagnetic behavior while no intersection is observed in the temperature range of 10 – 400 K, which reaffirms that T_c

is higher than 400 K. However, the FC/ZFC curves of the Mn-ZnO NWs show the blocking temperature at $T_b = 90$ K. Because it is also observed from ZFC/FC curves of the as-grown ZnO NWs ($T_b = 50$ K), as shown in Supporting Information Figure S3a, the existence of the blocking temperature may result from intrinsic defects, such as oxygen vacancy,^{33,34} which contribute to a weak intrinsic ferromagnetism though the ferromagnetism is significantly enhanced after the Mn-doping, as shown in Supporting Information Figure S3b. In Figure 4d, the bifurcation begins to increase as the temperature goes below 100 K, and the effect of the external magnetic field starts to overcome the thermal fluctuation and dominate the overall magnetization when the temperature is lower than 100 K. This trend is roughly consistent with the following magneto-transport measurements, in which the MR ratio of a single Mn-ZnO NW in the Figure 5b also quickly increases while the temperature is lower than 50 K.

The temperature-dependent magneto-transport measurements on a back-gated Mn-ZnO NW FET were carried out in a Quantum Design physical property measurements system (PPMS). To exclude the contact resistance, a standard four-probe setup was used to measure the channel resistance with a Keithley 6221 DC/AC current source and a Keithley 2182 nanovoltmeter. Figure 5a shows the temperature-dependent resistance (R - T) measurements on a single Mn-ZnO NW under an axial magnetic field of $H_{||} = 9$ T (solid square) and $H = 0$ T (open circle), respectively. The axial magnetic field was applied along the NW, as shown in the inset of Figure 3b. To further investigate carrier-mediated ferromagnetism in Mn-ZnO material system, the impurity band model from Coey et al.⁹ is considered to explain the long-range magnetic order at a low Mn concentration (~ 1 atom %). In their model, the FM in dilute ferromagnetic oxide is mediated by shallow donor electrons, which form bound magnetic polarons and overlap to create a spin-split impurity band. Because this model relies on thermal activated carriers, the zero field R - T curve in the inset of Figure 5a is fitted using modified Arrhenius law under the polaron assumption:^{12,35}

$$R(T) = R_0 T^\alpha \exp\left(\frac{E_a}{kT}\right) \quad (3)$$

where $\alpha = 3/2$ for a nonadiabatic polaron model.³⁵ The activation energy (E_a) of our Mn-ZnO NW was estimated to be approximately 33 meV, which is close to the value of 42.4 meV reported from the Mn-ZnO thin film.¹² Figure 5b shows the MR ratio as a function of axial magnetic field at different temperature ($T = 1.9$ –50 K). The curves are intentionally shifted for the purpose of clarity, and the length of double side arrow represents the 10 % change of the MR ratio. The height of MR peak is about 8 % at 1.9 K, and it is observable up to 50 K. These positive MR indicate the presence of spin-dependent scattering, which has been reported previously that the giant spin-splitting of the impurity band in Mn-ZnO affects the quantum correction to resistivity and turns the MR behavior from weak localization to weak antilocalization.^{36,37} In our Mn-ZnO NW system, the low temperature ($T < 50$ K) MR is proportional to the magnetization. However, it also depends on the effect of spin-dependent scattering, which is associated with the phase coherence length that has a strong temperature dependence of $L_\phi(T) \sim T^{-1/2}$.³⁷ The value of MR drops with raising temperature, and is easily overwhelmed by the thermal

noise at higher temperature. Therefore the MR is only detected at low temperature ($T < 50$ K) in our Mn-ZnO NWs.

Although most research focuses on the Mn-ZnO thin films, it is particular interest to investigate the electric-field control of FM in nanostructures, because the quantum confinement could significantly enhance the exchange coupling between the confined carriers and the localized Mn^{2+} .^{4,38} Figure 5c shows the MR ratio as a function of axial magnetic field under different gate voltages ($V_g = -40$ –40 V), where ΔMR is defined as the height of the MR curves and extracted by averaging the MR value within the saturation region ($H_{||} = 8$ –9 T). Figure 5d summarizes the gate modulation of the MR measurements. The left (right) axis shows the ΔMR (zero-field resistance, $R_{H=0}$) as a function of the gate voltage, respectively. The gate-dependence of $R_{H=0}$ in Figure 5d suggests that the electron density increases as the gate voltage increases. As predicted by the impurity band model for carrier-mediated ferromagnetism in diluted ferromagnetic oxide,⁹ increasing itinerant electron concentration would enhance the interaction between each polarons, and hence increase the magnetism. This enhanced magnetism is evidenced by the electric-field modulation of MR ratio, which also increases from 5.6 to 8.1 % when the gate voltage increases from -40 to $+40$ V. Therefore, our results are consistent with the carrier-mediated ferromagnetism model⁹ in Mn-ZnO system. Although this work shows that the electric-field modulation of magnetic moment is only observed at low temperature, it is the first demonstration of electric-field modulation of magnetism of diluted magnetic ZnO NWs.

Conclusions. In this paper, the Mn-ZnO NWs were synthesized by a gas-phase surface diffusion process in a dedicated MBE system. The Mn concentration was estimated to be $x_{\text{Mn}} = 1$ atom %. The presence of Mn precipitates was not observed based on XPS, XRD, and SEM experiments. The perfect crystalline of the Mn-ZnO NWs was confirmed by HR-TEM. Room-temperature FET characterization shows that majority carrier was n-type, and the corresponding mobility (carrier concentration) was $0.65 \text{ cm}^2/\text{V}\cdot\text{s}$ ($6.82 \times 10^{18} \text{ cm}^{-3}$), respectively. Curie temperature of Mn-ZnO NWs was estimated to be about 437 K from SQUID measurements. The difference of ΔMR is up to 2.5 % as the gate voltage changes from -40 to $+40$ V at $T = 1.9$ K, which suggests the electric-field control of ferromagnetism. The successful demonstration of gate modulation of FM in a DMS NW represents an important step toward realizing future all-spin logic devices.

■ ASSOCIATED CONTENT

Supporting Information

Additional information and figures. This material is available free of charge via the Internet at <http://pubs.acs.org>.

■ AUTHOR INFORMATION

Corresponding Authors

*E-mail: (K.L.W.) wang@seas.ucla.edu.

*E-mail: (L.-J.C.) ljchen@mx.nthu.edu.tw.

Author Contributions

^{||}C.-Y.W and J.T. had equal contribution.

Notes

The authors declare no competing financial interest.

■ ACKNOWLEDGMENTS

This work was in part supported by Western Institution of Nanoelectronics (WIN) and the Focus Center on Functional Engineered Nano Architectonics (FENA). The authors also acknowledged the support from National Science Council through Grants No. NSC 102-2221-E-007-145 and NSC 103-2218-E-011-007-MY3, and National Science Foundation ECCS 1308358.

■ REFERENCES

- (1) Wolf, S. A.; Awschalom, D. D.; Buhrman, R. A.; Daughton, J. M.; Molnar, S. v.; Roukes, M. L.; Chtchelkanova, A. Y.; Treger, D. M. *Science* **2001**, *294*, 1488–1495.
- (2) Datta, S.; Das, B. *Appl. Phys. Lett.* **1990**, *56*, 665–667.
- (3) Sugahara, S.; Tanaka, M. *Appl. Phys. Lett.* **2004**, *84*, 2307–2309.
- (4) Xiu, F.; Wang, Y.; Kim, J.; Hong, A.; Tang, J.; Jacob, A. P.; Zou, J.; Wang, K. L. *Nat. Mater.* **2010**, *9*, 337–344.
- (5) Tang, J.; Wang, C.-Y.; Chang, L.-T.; Fan, Y.; Nie, T.; Chan, M.; Jiang, W.; Chen, Y.-T.; Yang, H.-J.; Tuan, H.-Y.; Chen, L.-J.; Wang, K. L. *Nano Lett.* **2013**, *13*, 4036–4043.
- (6) Dietl, T.; Ohno, H.; Matsukura, F.; Cibert, J.; Ferrand, D. *Science* **2000**, *287*, 1019–1022.
- (7) Sharma, P.; Gupta, A.; Rao, K. V.; Owens, F. J.; Sharma, R.; Ahuja, R.; Guillen, J. M. O.; Johansson, B.; Gehring, G. A. *Nat. Mater.* **2003**, *2*, 673–677.
- (8) Kundaliya, D. C.; Ogale, S. B.; Lofland, S. E.; Dhar, S.; Metting, C. J.; Shinde, S. R.; Ma, Z.; Varughese, B.; Ramanujachary, K. V.; Salamanca-Riba, L.; Venkatesan, T. *Nat. Mater.* **2004**, *3*, 709–714.
- (9) Coey, J. M. D.; Venkatesan, M.; Fitzgerald, C. B. *Nat. Mater.* **2005**, *4*, 173–179.
- (10) Venkatesan, M.; Fitzgerald, C. B.; Lunney, J. G.; Coey, J. M. D. *Phys. Rev. Lett.* **2004**, *93*, 177206.
- (11) Yang, Z.; Liu, J. L.; Biasini, M.; Beyermann, W. P. *Appl. Phys. Lett.* **2008**, *92*, 042111.
- (12) Mukherjee, D.; Dhakal, T.; Srikanth, H.; Mukherjee, P.; Witanachchi, S. *Phys. Rev. B* **2010**, *81*, 205202.
- (13) Philipose, U.; Nair, S. V.; Trudel, S.; de Souza, C. F.; Aouba, S.; Hill, R. H.; Ruda, H. E. *Appl. Phys. Lett.* **2006**, *88*, 263101.
- (14) Zhong Lin, W. J. *Phys.: Condens. Matter* **2004**, *16*, R829–R858.
- (15) Bates, C. H.; White, W. B.; Roy, R. J. *Inorg. Nucl. Chem.* **1966**, *28*, 397–405.
- (16) Afsal, M.; Wang, C.-Y.; Chu, L.-W.; Ouyang, H.; Chen, L.-J. *J. Mater. Chem.* **2012**, *22*, 8420–8425.
- (17) Garnett, E. C.; Tseng, Y.-C.; Khanal, D. R.; Wu, J.; Bokor, J.; Yang, P. *Nat. Nanotechnol.* **2009**, *4*, 311–314.
- (18) Ford, A. C.; Chuang, S.; Ho, J. C.; Chueh, Y.-L.; Fan, Z.; Javey, A. *Nano Lett.* **2010**, *10*, 509–513.
- (19) Yang, Z.; Zuo, Z.; Zhou, H. M.; Beyermann, W. P.; Liu, J. L. *J. Cryst. Growth* **2011**, *314*, 97–103.
- (20) Wagner, C. D.; Davis, L. E.; Zeller, M. V.; Taylor, J. A.; Raymond, R. H.; Gale, L. H. *Surf. Interface Anal.* **1981**, *3*, 211–225.
- (21) Biesinger, M. C.; Payne, B. P.; Grosvenor, A. P.; Lau, L. W. M.; Gerson, A. R.; Smart, R. S. C. *Appl. Surf. Sci.* **2011**, *257*, 2717–2730.
- (22) Reeber, R. R. *J. Appl. Phys.* **1970**, *41*, 5063–5066.
- (23) Heiland, G.; Kunstmann, P. *Surf. Sci.* **1969**, *13*, 72–84.
- (24) Oba, F.; Togo, A.; Tanaka, I.; Paier, J.; Kresse, G. *Phys. Rev. B* **2008**, *77*, 245202.
- (25) Brillson, L. J.; Lu, Y. *J. Appl. Phys.* **2011**, *109*, 121301–33.
- (26) Tang, J.; Wang, C.-Y.; Hung, M.-H.; Jiang, X.; Chang, L.-T.; He, L.; Liu, P.-H.; Yang, H.-J.; Tuan, H.-Y.; Chen, L.-J.; Wang, K. L. *ACS Nano* **2012**, *6*, 5710–5717.
- (27) Tang, J.; Wang, C.-Y.; Xiu, F.; Lang, M.; Chu, L.-W.; Tsai, C.-J.; Chueh, Y.-L.; Chen, L.-J.; Wang, K. L. *ACS Nano* **2011**, *5*, 6008–6015.
- (28) Kim, H.-K.; Kim, S.-W.; Yang, B.; Kim, S.-H.; Lee, K. H.; Ji, S. H.; Yoon, Y. S. *Jpn. J. Appl. Phys.* **2006**, *45*, 1560.
- (29) Jacobi, K.; Zwicker, G.; Gutmann, A. *Surf. Sci.* **1984**, *141*, 109–125.
- (30) Arrott, A. *Phys. Rev.* **1957**, *108*, 1394–1396.
- (31) Stanley, H. E. *Introduction to Phase Transitions and Critical Phenomena*; Oxford: New York, 1971.
- (32) Camprostrini, M.; Hasenbusch, M.; Pelissetto, A.; Rossi, P.; Vicari, E. *Phys. Rev. B* **2002**, *65*, 144520.
- (33) Choudhury, B.; Choudhury, A.; Maidul Islam, A. K. M.; Alagarsamy, P.; Mukherjee, M. *J. Magn. Magn. Mater.* **2011**, *323*, 440–446.
- (34) Wang, Q.; Sun, Q.; Chen, G.; Kawazoe, Y.; Jena, P. *Phys. Rev. B* **2008**, *77*, 205411.
- (35) Jiang, W.; Zhou, X. Z.; Williams, G.; Mukovskii, Y.; Glazyrin, K. *Phys. Rev. B* **2008**, *78*, 144409.
- (36) Dietl, T.; Andrearczyk, T.; Lipińska, A.; Kiecana, M.; Tay, M.; Wu, Y. *Phys. Rev. B* **2007**, *76*, 155312.
- (37) Andrearczyk, T.; Jaroszyński, J.; Grabecki, G.; Dietl, T.; Fukumura, T.; Kawasaki, M. *Phys. Rev. B* **2005**, *72*, 121309.
- (38) Chen, J.; Wang, K. L.; Galatsis, K. *Appl. Phys. Lett.* **2007**, *90*, 012501.